coatings

MDPI

Article

Influence of Different Rotations of Organic Formamidinium Molecule on Electronic and Optical Properties of $FAPbBr_3$ Perovskite

Abdullah A. Al-Kahtani [1], Sobia Tabassum [2,*], Indah Raya [3], Ibrahim Hammoud Khlewee [4], Supat Chupradit [5], Afshin Davarpanah [6], Marischa Elveny [7,*] and Shafaqat Ali [8,9,*]

1 Chemistry Department, College of Science, King Saud University, P.O. Box 2455, Riyadh 11451, Saudi Arabia; akahtani@ksu.edu.sa
2 Department of Biological Sciences, International Islamic University, H-10 Campus, Islamabad 44000, Pakistan
3 Departement of Chemistry, Faculty Mathematics and Natural Science, Hasanuddin University, Makassar 90245, Indonesia; indahraya@unhas.ac.id
4 Department of Prosthodontics, College of Health and Medical Technololgy, Al-Ayen University, Nasiriyah 64011, Iraq; ibrahim.khlewee@alayen.edu.iq
5 Department of Occupational Therapy, Faculty of Associated Medical Sciences, Chiang Mai University, Chiang Mai 50200, Thailand; supat.c@cmu.ac.th
6 Chemistry of Interfaces, Luleå University of Technology, SE-97187 Luleå, Sweden; afshindpe@gmail.com
7 Data Science & Computational Intelligence Research Group, Universitas Sumatera Utara, Medan 20155, Indonesia
8 Department of Environmental Sciences and Engineering, Government College University, Allama Iqbal Road, Faisalabad 38000, Pakistan
9 Department of Biological Sciences and Technology, China Medical University, Taichung 40402, Taiwan
* Correspondence: sobia.tabasum@iiu.edu.pk (S.T.); marischaelveny@usu.ac.id (M.E.); shafaqataligill@yahoo.com (S.A.)

Abstract: Hybrid organic–inorganic halide perovskites (HOIPs) have recently represented a material breakthrough for optoelectronic applications. Obviously, studying the interactions between the central organic cation and the Pb-X inorganic octahedral could provide a better understanding of HOIPs. In this work, we used a first-principles theoretical study to investigate the effect of different orientations of central formamidinium cation (FA^+) on the electronic and optical properties of $FAPbBr_3$ hybrid perovskite. In order to do this, the band structure (with and without spin–orbit coupling (SOC)), density of states (DOS), partial density of states (PDOS), electron density, distortion index, bond angle variance, dielectric function, and absorption spectra were computed. The findings revealed that a change in the orientation of FA^+ caused some disorders in the distribution of interactions, resulting in the formation of some specific energy levels in the structure. The interactions between the inorganic and organic parts in different directions create a distortion index in the bonds of the inorganic octahedral, thus leading to a change in the volume of $PbBr_6$. This is the main reason for the variations observed in the electronic and optical properties of $FAPbBr_3$. The obtained results can be helpful in solar-cell applications.

Keywords: hybrid perovskites; formamidinium; distortion index; inorganic octahedral; bond angle variance; solar cell

check for updates

Citation: Al-Kahtani, A.A.; Tabassum, S.; Raya, I.; Khlewee, I.H.; Chupradit, S.; Davarpanah, A.; Elveny, M.; Ali, S. Influence of Different Rotations of Organic Formamidinium Molecule on Electronic and Optical Properties of $FAPbBr_3$ Perovskite. *Coatings* **2021**, *11*, 1341. https://doi.org/10.3390/coatings11111341

Academic Editors: Yingyi Zhang and Alessandro Latini

Received: 28 September 2021
Accepted: 26 October 2021
Published: 1 November 2021

Publisher's Note: MDPI stays neutral with regard to jurisdictional claims in published maps and institutional affiliations.

1. Introduction

Since the dawn of civilization, solar energy has been hailed as one of the most promising renewable energy resources [1–14]. By utilizing readily available materials and simple fabrication processes, thin-film technology promises to cut the cost of solar energy [15–28]. In recent years, a variety of light absorber materials have been studied in both organic and inorganic systems [29–42]. Due to their great processability, wide optical absorption cross-section, and good thermal stability [43–56], hybrid organic–inorganic halide perovskites

are regarded as being suitable materials for mesoscopic solar cells [57–72]. They have the general chemical formula ABX_3, where A is an organic/inorganic cation (e.g., Cs^+: cesium, $(CH_3NH_3)^+$: methylammonium, MA^+; $(CH(NH_2)_2)^+$: formamidinium, FA^+), X is a halogen anion (e.g., X = I^-, Br^-, Cl^-), and B is a divalent metal cation (e.g., Pb^{2+}) [73–77].

Changing the cations or anions in HOIPs can change their bandgap energy. For example, when iodide anions are substituted by a smaller halide, the bandgap increases [78–82]. While keeping the cubic structure, the bandgap reduces also upon substitution of formamidinium (FA) cation by smaller methylammonium (MA) cation [83–85]. FA-based lead bromide perovskite ($FAPbBr_3$) has been reported to have an optimum bandgap of ~2 eV, which translates to absorption up to 560 nm [86]. Altogether, it can be said that $FAPbBr_3$ could be a better active material than $MAPbBr_3$ for perovskite solar cells (PSCs) [87–90]. However, pure $FAPbBr_3$ has been discovered to be unstable because its trigonal-phase is sensitive to humidity and quickly transforms to a non-photoactive hexagonal-phase at room temperature [91–95].

In a wide range of molecular systems, such as organic and hybrid materials, molecule rotations play a key role in the dynamical and relaxation properties. In addition, in gases and liquids, the rotational disorder can also be seen in solid materials (e.g., hybrid perovskites) [96,97]. Several experimental techniques, including dielectric relaxation, infrared and Raman spectroscopy, spin relaxation, and fluorescence depolarization, have been used to offer information about the relaxation timeframes required to reestablish equilibrium after an appropriate perturbation of the molecular motion [98,99].

The organic cation formamidinium has an asymmetric charge distribution resulting in a net dipole moment. At temperatures around 330 K, $FAPbBr_3$ has a cubic structure, and the dipolar organic cation can rotate almost freely inside the metal-halide lattice [100–102]. This leads to a high dielectric screening compared to halide perovskites with non-dipolar cations, such as Cs^+ and Rb^+. The rotational freedom of organic cation has been found to be highly dependent on temperature. The dipolar nature of the central cation has a great effect on the optoelectronic properties of hybrid halide perovskites [100–102].

Moreover, it has been previously shown that $(CH(NH)_2)^+$ has no covalent bonding with the Pb-Br framework, which makes $(CH(NH)_2)^+$ more dynamic for various types of rotations [100,102].

In this work, we rotated organic FA cation in two axes within the $FAPbBr_3$ perovskite: (a) the vertical axis going through the C atom and (b) the connecting axis of N-N bond. Because the organic molecule was standing upright in the X direction, two rotation axes of Y and X were chosen with rotations at ideal angles of 15°, 30°, 45°, 60°, and 75°. DFT-based calculations were performed to investigate the influence of different rotations on the electronic and optical properties. We have supplied thorough information on the electrical and optical performance of $FAPbBr_3$ at different angles. The findings could help researchers figure out which structure is suitable for use in solar cells.

2. Computational Details

Quantum Espresso's PWSCF Code was used for all calculations [103]. The generalized gradient approximation (GGA) was used in the scheme of Perdew–Burke–Ernzerhof (PBE) [104] to describe the exchange-correlation functional. We focused on the rotation of organic cation (FA^+) within the pseudo-cubic phase of $FAPbBr_3$ perovskite. The density of valence electrons and wave functions were also represented by using scalar relativistic ultra-soft and plane-wave basis set pseudo-potentials. The energy cutoffs of wave functions and electron density were set to be 37 and 365 Rydberg, respectively. The Brillouin zone (BZ) of the cubic systems was sampled by using a 10 × 10 × 10 Monkhorst–Pack grid [105,106]. The structure was fully relaxed until the force on each atom was less than 0.0051 eV A^{-1}. The frequency-dependent complex dielectric function was computed by using the following equation [103]:

$$\varepsilon(\omega) = 1 + \frac{8\pi}{\Omega N_k} \sum_{k,v,c} \frac{|\langle \varphi_{kv}|\hat{v}|\varphi_{kc}\rangle|^2}{(E_{kc} - E_{kv})^2 (E_{kc} - E_{kv} - \omega - i\eta)} \quad (1)$$

where Ω is the cell volume, N_k represents total number of k-points in the BZ, $\hat{v}$ is the velocity operator, and η is an opportune broadening factor. The indices v and c denote the occupied and unoccupied states, respectively.

It is feasible to acquire the whole dielectric tensor evaluated on the imaginary frequency axe $\varepsilon(i\omega)$ by applying a London transformation on $\varepsilon_i(\omega)$ [103].

$$\varepsilon(i\omega) = 1 + \frac{2}{\pi}\int_0^\infty \frac{\omega'\varepsilon_i(\omega')}{\omega\prime^2 + \omega^2}d\omega \tag{2}$$

The electron energy-loss spectrum (EELS), which is proportional to the imaginary of the inverse dielectric tensor, was obtained by using the relation [103];

$$\mathrm{Imm}\left\{\frac{1}{\varepsilon(\omega)}\right\} = \frac{\varepsilon_i(\omega)}{\varepsilon_r^2(\omega) + \varepsilon_i^2(\omega)} \tag{3}$$

The frequency-dependent absorption coefficient, $\alpha(\omega)$, was determined by using the following formula:

$$\alpha(\omega) = \omega\sqrt{\frac{-\varepsilon_r(\omega) + \sqrt{\varepsilon_r^2(\omega) + \varepsilon_i^2(\omega)}}{2}} \tag{4}$$

3. Results

Inside a cubic structure of hybrid perovskite, the organic Formamidinium (FA) cation is situated in the X (100) direction (pm3m). The rotational modes of FA^+ within the $PbBr_6$ inorganic octahedral are schematically depicted in Figure 1a. Figure 1b also displays the position of FA^+ and $PbBr_6$ octahedral in the structure of $FAPbBr_3$ perovskite. In order to get a clear vision from the FA behavior inside the Pb-Br framework, six different angles, namely 0°, 15°, 30°, 45°, 60°, and 75°, were considered regarding both Y and X axes.

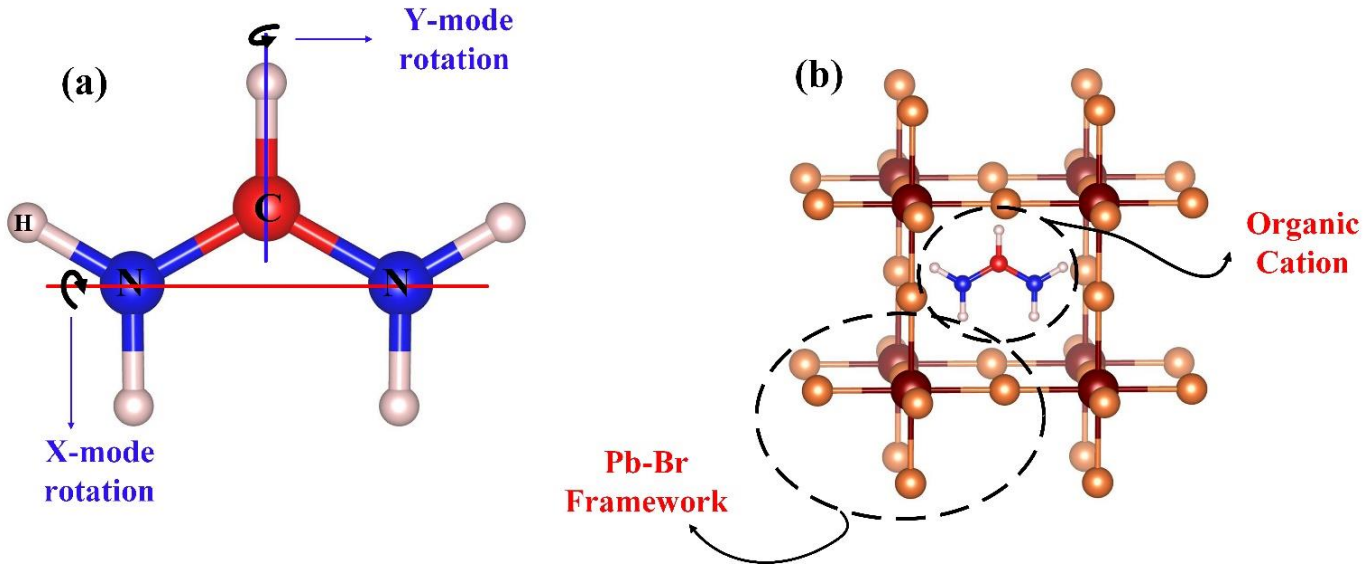

Figure 1. (**a**) Rotational modes of cation FA within the structure of $FAPbBr_3$ perovskite. (**b**) Position of cation FA and Pb-Br framework within the structure.

Table 1 and Figure 2l represent the computed bandgaps for different rotational modes. As can be seen, from 15° to 75°, the lattice parameter of the $FAPbBr_3$ in Y mode exhibits a valley-like behavior (solid red line in Figure 2l).

Table 1. Lattice parameters and bandgaps (with and without SOC) of $FAPbBr_3$ perovskite for all rotational modes.

Rotational Mode	Lattice Parameter (Å)	Bandgap without SOC (eV)	Bandgap with SOC (eV)
0°-X	5.97	1.61	0.40
15°-Y	5.93	1.65	0.62
30°-Y	5.89	1.70	0.65
45°-Y	5.81	1.79	1.35
60°-Y	5.85	1.73	1.04
75°-Y	5.91	1.68	0.72
15°-X	5.96	1.62	0.49
30°-X	5.94	1.64	0.55
45°-X	5.90	1.72	0.98
60°-X	5.92	1.66	0.61
75°-X	5.95	1.63	0.52

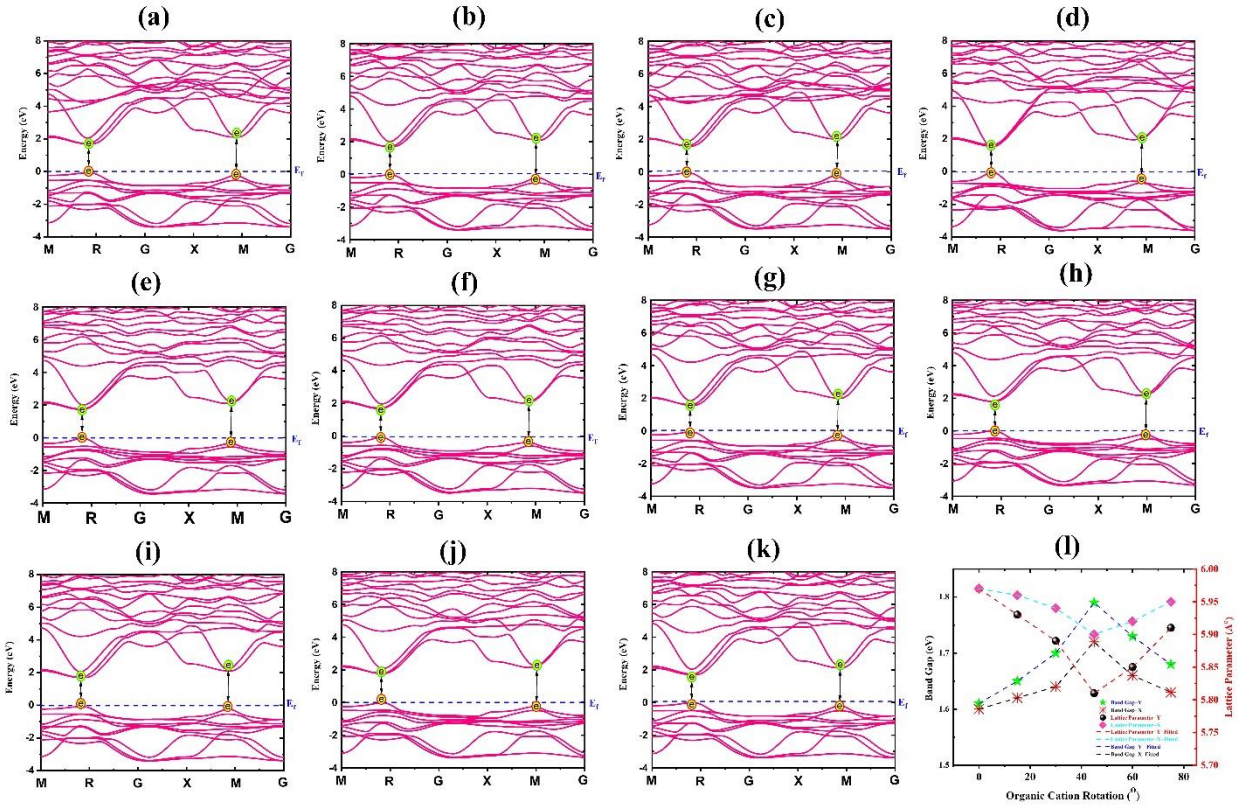

Figure 2. Calculated band structure of $FAPbBr_3$ perovskite without SOC for rotational modes of (**a**) 0°-X, (**b**) 15°-Y, (**c**) 30°-Y (**d**) 45°-Y, (**e**) 60°-Y, (**f**) 75°-Y, (**g**) 15°-X, (**h**) 30°-X, (**i**) 45°-X, (**j**) 60°-X and (**k**) 75°-X. (**l**) Variations of bandgap and lattice parameter in term of rotational orientation.

The significant decrease in the lattice parameter from 15° to 75° indicates a decrease in the structure volume. From Table 1, it is evident that 45°-rotated FA leads to the smallest unite cell for $FAPbBr_3$. Calculations on X-rotated FA, however, show that the variation of lattice parameter in this mode is small (less than 0.07 A°). This can be attributed to the fixed positions of NH_2 and NH_2 for X rotational modes (see Figure 2l). On the other hand, we may deduce from the computed band structures and energy bandgaps that the bandgap and the lattice parameter have a direct relationship as a function of rotational orientation. The bandgap energies of $FAPbBr_3$ increased to a maximum of 1.79 eV (45° Y-rotated values) from 1.61 eV (non-rotated data). As a result, we can say with certainty that decreasing the structure size (as determined by the lattice parameter) causes an increase in the organic

cation and inorganic octahedral interaction radius, pushing the conduction band to higher energies. Figure 2 depicts the band structure of $FAPbBr_3$ perovskite for rotational angles of 0°, 15°, 30°, 45°, 60°, and 75° in both Y and X modes. The band structure corresponding to the stable 0°-rotated FA for $FAPbBr_3$ is shown in Figure 2a. A direct bandgap was discovered at the points R and M of BZ (shown with yellow and green dots). The band degeneracy is observed at points R and M in the CBM. The band structures in which the organic cation $(CH(NH_2)_2)^+$ rotates in Y mode with an angle of 45° is represented by Figure 2d. The bands stay direct at high-symmetry R and M points despite FA^+ rotation.

Furthermore, we may deduce from Figure 2 that changes in the structure volume affect the interaction between organic cation and inorganic octahedra and as a result cause considerable changes in the band structure.

Figure 2g–k illustrates the band structures related to the rotation of FA^+ in X mode, demonstrating a direct bandgap at the R and M points of BZ. Unlike traditional semiconductors, such as GaAs, which have a dual-degeneracy at Γ point of VBM, but $FAPbBr_3$ structure has a triple degeneracy at R point of CBM in BZ. The orientational disorders of organic cations in HOIPs cause this fundamental divergence. It is worth noting that organic cation does not have a direct role in VBM and CBM. However, the size, shape, and position of organic cations inside the Pb-Br framework have a considerable effect in the electronic and optical properties of HOIPs. The rotation of FA in Y and X modes affects the band structure while maintaining its original shape at the R point of BZ. Organic cations interact with the inorganic octahedral, which results in the change of band structure.

The presence of d orbital of lead atom in the HOIPs structure makes the spin–orbit coupling (SOC) effect remarkable. Therefore, the band structure and bandgap (Eg) size were calculated taking into account this effect, as shown in Figure 3 and Table 1.

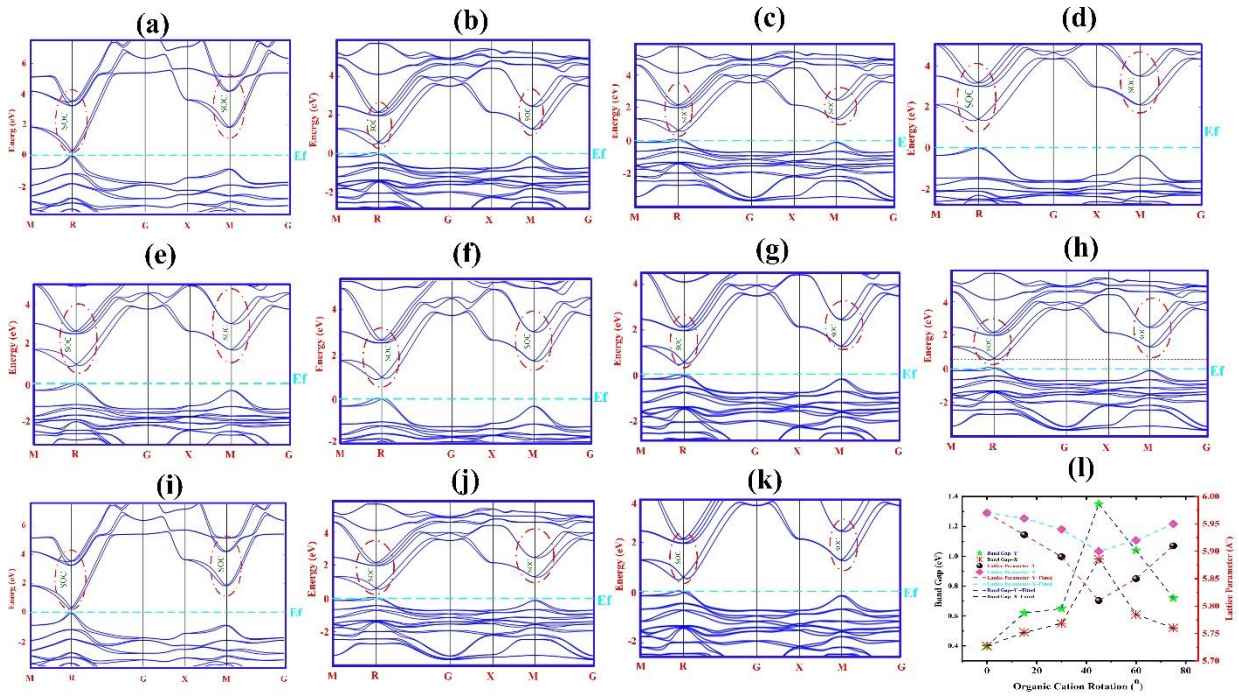

Figure 3. Calculated band structure of $FAPbBr_3$ perovskite with SOC for rotational modes of (**a**) 0°-X, (**b**) 15°-Y, (**c**) 30°-Y (**d**) 45°-Y, (**e**) 60°-Y, (**f**) 75°-Y, (**g**) 15°-X, (**h**) 30°-X, (**i**) 45°-X, (**j**) 60°-X and (**k**) 75°-X. (**l**) Variations of bandgap and lattice parameter in term of rotational orientation. SOC is shown with red dashed line in CBM.

According to Figure 3, considering the SOC effect, for HOIPs at R and M points of CBM, degeneracy leads to a non-degenerate state at the CBM. For HOIPs while maintaining double degeneracy at transition point M, there is a band splitting from triple to double at transition point R. In fact, due to the presence of d orbital of lead atom and since the

most of the conduction band is affected by the lead atom, the band splitting occurs in the conduction band and a red shift appears in the CBM.

Figure 4 depicts electron density of $FAPbBr_3$ structure in 2D representation from the crystallographic planes. It appears that interacting $(CH(NH_2)_2)^+$ with $PbBr_6$ octahedral, results in some structural disorders that alters the octahedral volume as well as the total volume of the structure (refer to Table 1 and Figure 5).

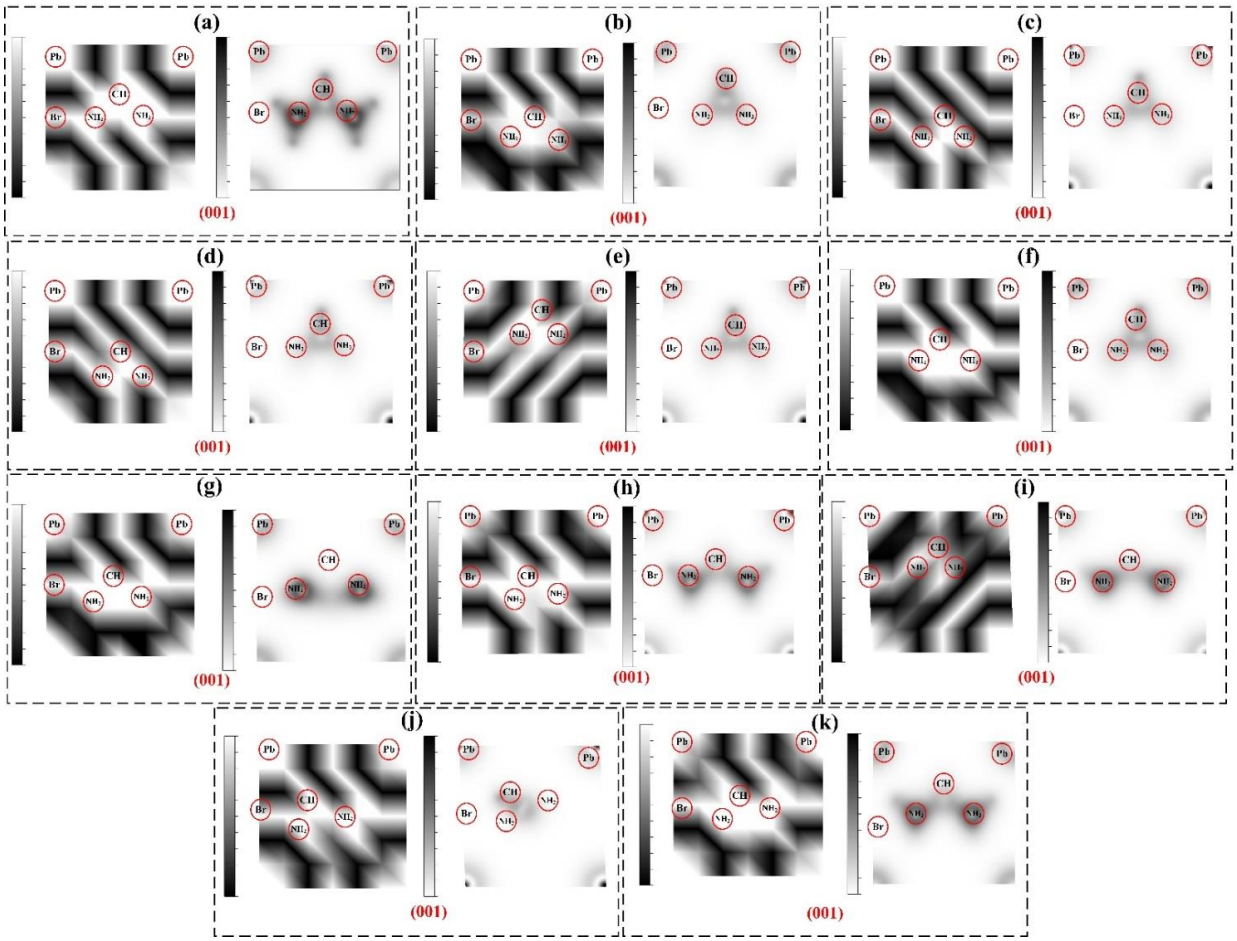

Figure 4. Two-dimensional depiction of electron density of $FAPbBr_3$ perovskite for rotational modes of: (**a**) 0°-X, (**b**) 15°-Y, (**c**) 30°-Y (**d**) 45°-Y, (**e**) 60°-Y, (**f**) 75°-Y, (**g**) 15°-X, (**h**) 30°-X, (**i**) 45°-X, (**j**) 60°-X and (**k**) 75°-X.

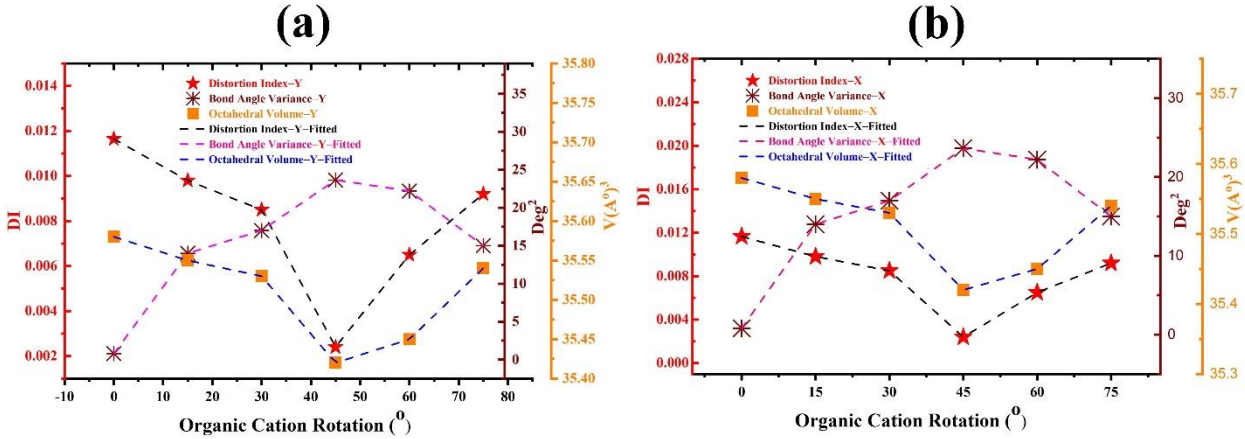

Figure 5. Calculated average distortion index (bond length), bond-angle variance, and average octahedra volume of $FAPbBr_3$ perovskite for different FA rotations: (**a**) in Y mode and (**b**) in X mode.

Due to the relatively greater ionic radius of NH_2, its interaction is substantially higher than that of CH, as shown in Figure 4's 2D counter plots in (001) plane and also Table 2. On the basis of rotational angles, the average distortion index (bond length), bond angle variance and volume of the octahedral were calculated and shown in Figure 5. When FA is rotated, the interaction between the FA^+ and $PbBr_6$ is greatly enhanced (see (001) plane in Figure 4). As shown in Figure 5a, the average volume of the octahedral is reduced, leading to an increase of the bandgap energy (refer to Figure 2).

Table 2. Ionic radii; atomic radii; Van Der Waals radii; and atomic masses of I, Pb, N, C, and Br.

Atom Name	Ionic Radius (A°)	Atomic Radius (A°)	Van der Waals Radius (A°)	Atomic Mass
Br	1.96	1.14	1.85	79.90
N	1.46	0.74	1.55	14.00
C	0.15	0.77	1.70	12.01
Pb	1.19	1.75	2.16	207.20
H	0.20	0.46	1.20	1.00

According to Figure 5, it is clear that, at a rotation angle of 45° for both rotation axes Y and X, the bond angle variance of $PbBr_6$ inorganic octahedral is maximized. This is a direct result of the reduced volume of $PbBr_6$ at 45°.

We can conclude from this section that the distance and radius of interaction between the inorganic octahedral and the organic cation could be regarded as controlling tools of electron density and bandgap energies. The electron density of the structure was calculated regarding the rotational mode of 30°-X on the (001) plane, indicating no significant changes in comparison to the FA-0°X (Figure 4a). The reason for this could be related to the fixed positions of N atoms and the only displacement of CH in the X rotational mode. Thus, the existence of FA organic cation formed from two distinct ionic radii (CH and NH_2) is the main reason of the structural disorders in $FAPbBr_3$ perovskites. FA plays a significant role in cation–cation (FA^+–Pb^{2+}) and cation–onion (FA^+–Br^-) molecular interactions in HOIP structure.

We calculated total DOS and PDOS, as illustrated in Figure 6. It depicts the contribution of atom valence orbitals in the structure for non-rotated and all rotated modes. Figure 6a corresponds to the PDOS of FA-0°x and shows that the VBM for the present system is dominated by 4p orbitals of Br and partly by 6s orbitals of Pb, and also the CBM is dominated by 6p orbitals of Pb atom. As can be seen, rotating FA from 0° to 75° in Y mode boosts the roles of 4p orbital of Br and 6p orbital of Pb in the valance and conduction bands, respectively. According to the electron-density data, the energy level of an organic cation in the (001) plane increases at these angles (compared to non-rotated states). This could be related to electron interactions between the p orbitals of lead and bromide atoms and those of organic cation. Notably, there is a blue shift in DOS of the conduction band at angles of 15°, 30°, 45°, 60°, and 75° when compared to non-rotated states. Energy states at 45°-Y show a greater variance than those at 15°-Y, 30°-Y, 60°-Y, and 75°-Y, which similarly influences the 6s and 6p orbitals of Pb at CBM. Due to the decreased structure volume and also the greater interactions between inorganic octahedral at 45°, CBM is moved to higher energies at this angle.

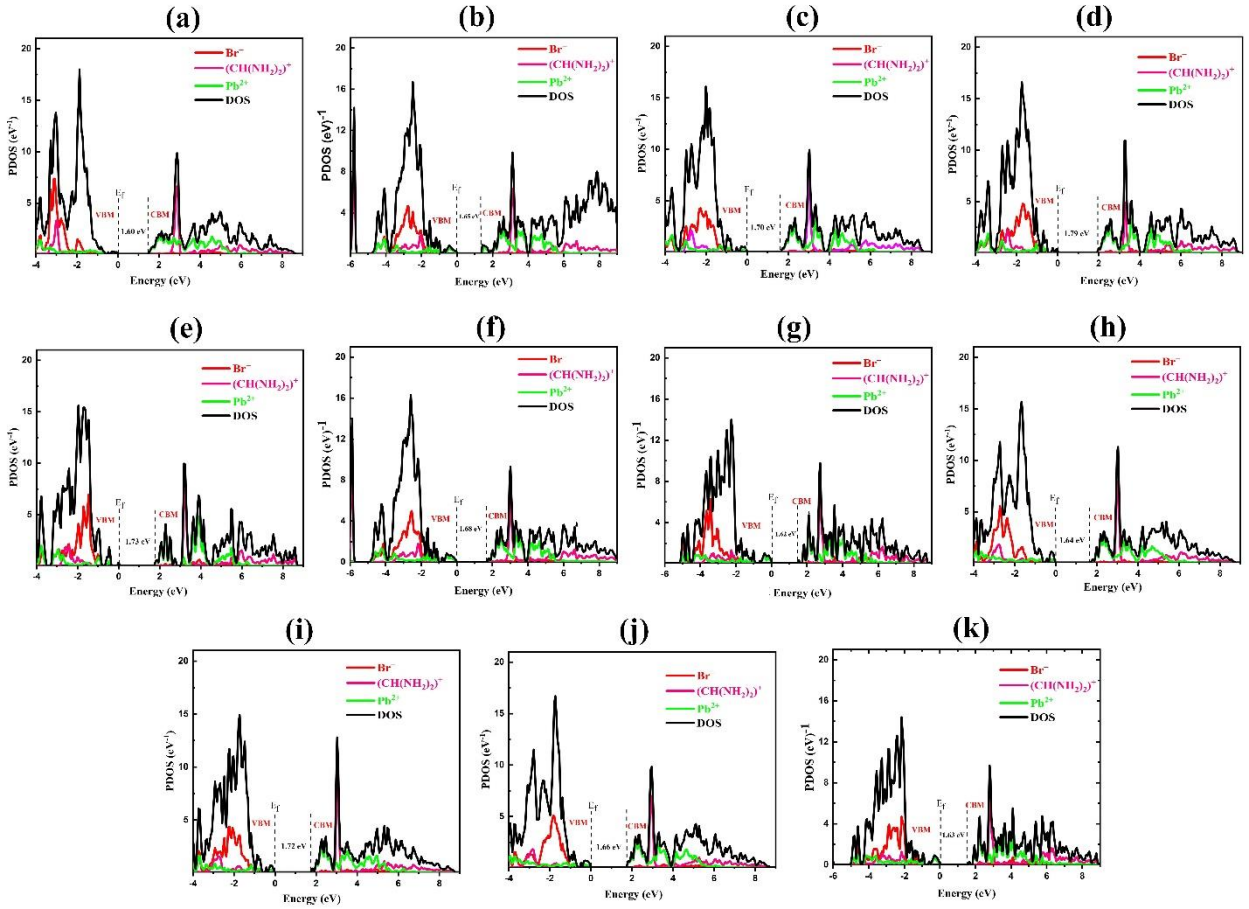

Figure 6. Calculated DOS and PDOS of $FAPbBr_3$ perovskite for rotational modes of (**a**) 0°-X, (**b**) 15°-Y, (**c**) 30°-Y (**d**) 45°-Y, (**e**) 60°-Y, (**f**) 75°-Y, (**g**) 15°-X, (**h**) 30°-X, (**i**) 45°-X, (**j**) 60°-X and (**k**) 75°-X.

From Figure 6g–k, it is clear that, similar to the Y mode, a change in the orientation of FA in the X mode leads to the change of PDOS.

We calculated the dielectric function for the $FAPbBr_3$ structure in FA-0°, Y, and X rotating modes (see Figures 7–9 and Table 3). The real parts of the dielectric function for Y mode rotations are shown in Figure 7a. As a result, for non-rotated FA, the static dielectric constant at E = 0 is predicted to be 6.31. Nonetheless, when the FA is rotated in the Y mode, the static dielectric constant of the structure increases at all rotational angles. Moreover, Figure 8 shows the imaginary parts of the dielectric function. The first peak in these spectra represents the direct optical transition known as the optical gap (R transition point in BZ). For the non-rotated case, this peak is positioned at 1.61 eV. The peak also experiences a blue shift when the FA organic cation is rotated at all angles. In addition, the effect of FA rotation with X mode is displayed in Figure 7b, which shows a different result than Y with a significant change in static dielectric constant.

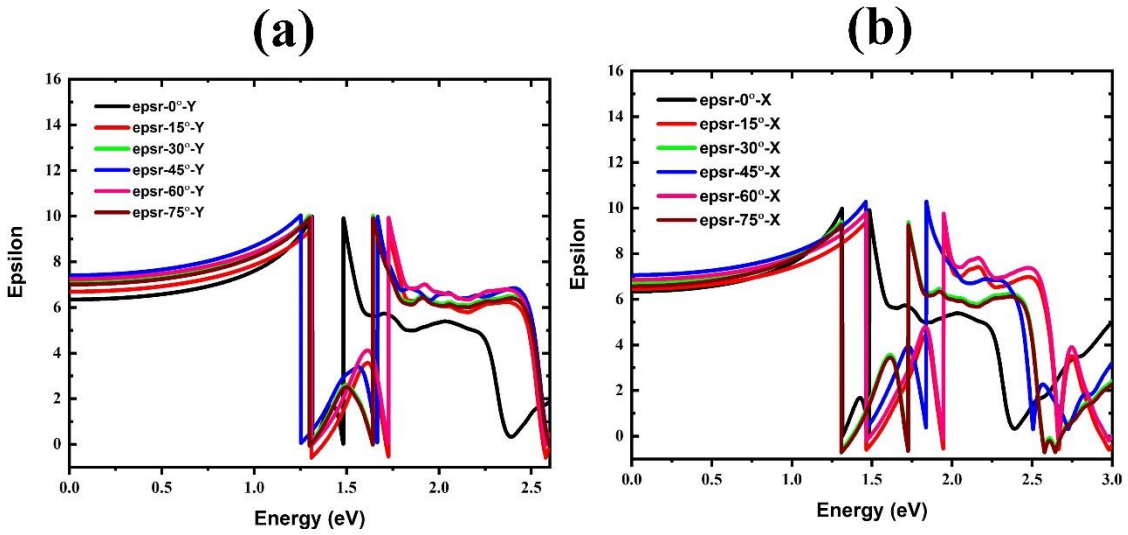

Figure 7. Real part of dielectric function of $FAPbBr_3$ perovskite for different FA rotations: (**a**) in Y mode and (**b**) in X mode.

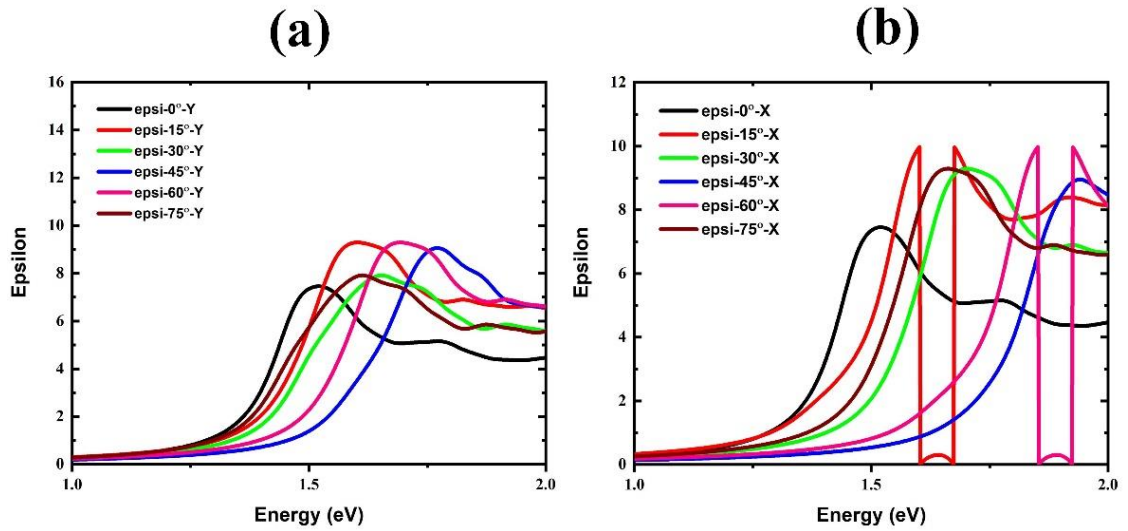

Figure 8. Imaginary part of dielectric function of $FAPbBr_3$ perovskite for different FA rotations: (**a**) in Y mode and (**b**) in X mode.

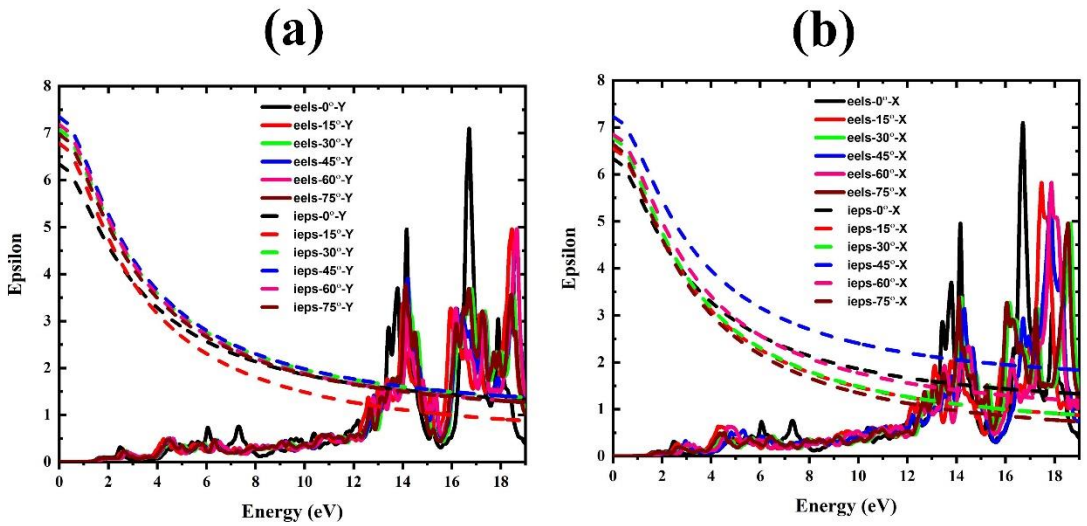

Figure 9. Electron energy loss and $\varepsilon(i\omega)$ spectra of $FAPbBr_3$ perovskite for different FA rotations: (**a**) in Y mode and (**b**) in X mode.

Table 3. Wavelength of absorption edge and static dielectric constants of $FAPbBr_3$ perovskite for all rotational modes.

Rotational Mode	ε_0	α (nm)
0°-X	6.31	770
15°-Y	6.73	751
30°-Y	7.07	729
45°-Y	7.34	692
60°-Y	7.27	716
75°-Y	7.04	738
15°-X	6.35	765
30°-X	6.50	756
45°-X	7.04	720
60°-X	6.75	746
75°-X	6.40	760

From the large changes in the positions of NH_2 and CH molecules, it can be concluded that rotating FA with Y mode increases cation–cation (FA^+–Pb^{2+}) and cation–onion (FA^+–Br^-) interactions. As a result, it can be inferred that the dielectric function of the system varies by changing the structure size and bandgap value at all rotational modes.

To confirm the accuracy of the static dielectric constant calculations, the $\varepsilon(i\omega)$ spectrum was evaluated for all rotational modes and shown in Figure 9. It is clear that the starting point of these spectra actually corresponds to the static dielectric constant. According to the electron energy-loss spectra (Figure 9), it is observed that, at the location of the first peak, there is the least amount of electron energy loss, which is strong confirmation for the results obtained for the dielectric function.

The optical absorption spectra of $FAPbBr_3$ for FA-0° and rotational modes are shown in Figure 10a,b. For FA-0°, the absorption edge begins at 770 nm. Table 3 and Figure 10 provide detailed optical absorption data for Y and X modes, including blue-shifted absorption edges for all rotational modes. The largest change in absorption edge wavelength corresponds to a 45°-Y rotation (a blue shift of 78 nm). The smaller volume of the structure and the greater interactions between FA and Pb^{+2} result in a blue shift in the absorption spectrum at 45°-Y. The location and orientation of the organic cation, as well as its interaction with inorganic octahedra in various angles and directions, can potentially decrease the wavelength of the absorption edge, resulting in a tunable absorption spectrum for HOIP perovskites.

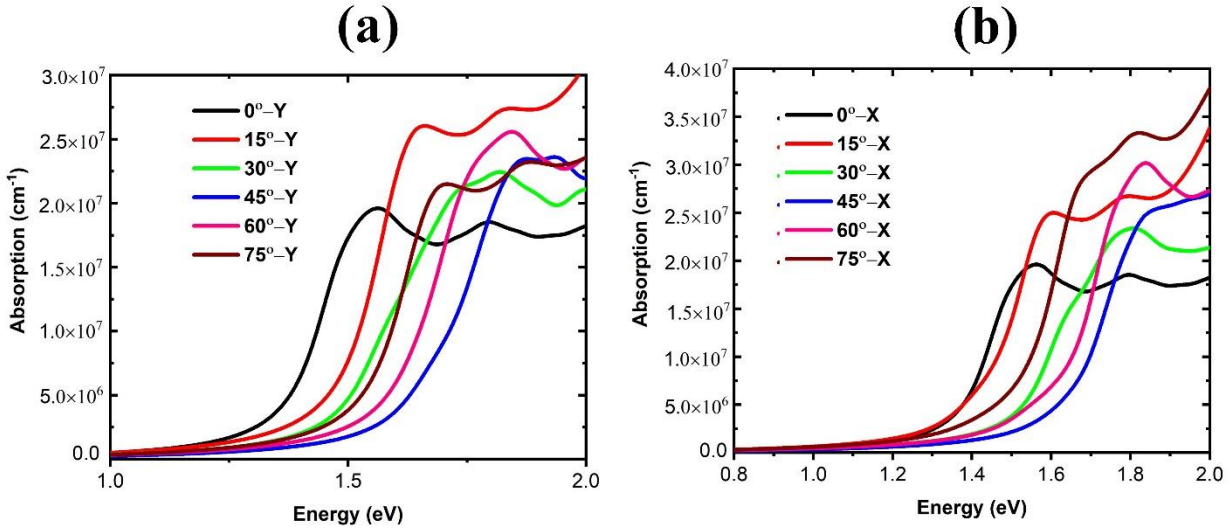

Figure 10. Optical adsorption spectrum of $FAPbBr_3$ perovskite for different FA rotations: (**a**) in Y mode and (**b**) in X mode.

4. Conclusions

The effect of different FA rotations was investigated on the band structure, electron density, DOS, dielectric function, and absorption spectra of $FAPbBr_3$. We found that FA has no direct contribution to the electronic band structure. However, due to the presence of cation–cation (FA^+–Pb^{2+}) and cation–anion (FA^+–Br^-) interactions within the structure of the $FAPbBr_3$, FA rotation changes the structural, electronic, and optical properties. The rotation of FA cation causes two important factors of distortion index and band-angle variance to affect the bonds of $PbBr_6$ inorganic octahedral. The influence of these factors in the structural properties of HOIPs, in turn, causes some changes in the electronic and optical properties. Modifying the rotational mode, position, and orientation of organic cations within the structure of a hybrid perovskite can be used for tuning the bandgap, static dielectric constant, and absorption edge.

Author Contributions: Conceptualization, A.A.A.-K. and S.T.; methodology, I.R.; software, M.E.; validation, A.A.A.-K., I.H.K. and S.C.; formal analysis, M.E.; investigation, S.A.; resources, A.A.A.-K.; data curation, S.T.; writing—original draft preparation, A.A.A.-K.; writing—review and editing, A.D.; visualization, I.R.; supervision, S.A.; project administration, A.A.A.-K.; funding acquisition, S.T. All authors have read and agreed to the published version of the manuscript.

Funding: This work was funded by the Researchers Supporting Project Number (RSP-2021/266) King Saud University, Riyadh, Saudi Arabia.

Institutional Review Board Statement: Not applicable.

Informed Consent Statement: Not applicable.

Data Availability Statement: Not applicable.

Conflicts of Interest: The authors declare no conflict of interest.

References

1. Bai, S.; Yuan, Z.; Gao, F. Colloidal metal halide perovskite nanocrystals: Synthesis, characterization, and applications. *J. Mater. Chem. C* **2016**, *4*, 3898–3904. [CrossRef]
2. Kojima, A.; Teshima, K.; Shirai, Y.; Miyasaka, T. Organometal halide perovskites as visible-light sensitizers for photovoltaic cells. *J. Am. Chem. Soc.* **2009**, *131*, 6050–6051. [CrossRef]
3. Yu, D.; Cao, F.; Gao, Y.; Xiong, Y.; Zeng, H. Room-temperature ion-exchange-mediated self-assembly toward formamidinium perovskite nanoplates with finely tunable, ultrapure green emissions for achieving rec. 2020 displays. *Adv. Funct. Mater.* **2018**, *28*, 1800248. [CrossRef]
4. Bi, D.; Tress, W.; Dar, M.I.; Gao, P.; Luo, J.; Renevier, C.; Schenk, K.; Abate, A.; Giordano, F.; Baena, J.-P.C. Efficient luminescent solar cells based on tailored mixed-cation perovskites. *Sci. Adv.* **2016**, *2*, e1501170. [CrossRef]
5. Yang, L.; Dai, Q.; Liu, L.; Shao, D.; Luo, K.; Jamil, S.; Liu, H.; Luo, Z.; Chang, B.; Wang, X. Rapid sintering method for highly conductive $Li_7La_3Zr_2O_{12}$ ceramic electrolyte. *Ceram. Int.* **2020**, *46*, 10917–10924. [CrossRef]
6. Zhu, W.; Deng, M.; Chen, D.; Zhang, Z.; Chai, W.; Chen, D.; Xi, H.; Zhang, J.; Zhang, C.; Hao, Y. Dual-phase $CsPbC_{13}$–Cs_4PbC_{l6} perovskite films for self-powered, visible-blind UV photodetectors with fast response. *ACS Appl. Mater. Interfaces* **2020**, *12*, 32961–32969. [CrossRef] [PubMed]
7. Sina, M.A.; Adeel, M.A. Assessment of stand-alone photovoltaic system and mini-grid solar system as solutions to electrification of remote villages in Afghanistan. *Int. J. Innov. Res. Sci. Stud.* **2021**, *4*, 92–99. [CrossRef]
8. Patel, S.R.; Parikh, S.P. Chromium removal from industrial effluent by electrocoagulation: Operating cost and kinetic analysis. *J. Environ. Treat. Tech.* **2021**, *9*, 621–628. [CrossRef]
9. Laaziz, A.; Kouda, I.; Barhoun, A.; Draoui, K. Kinetic, isotherm and thermodynamic study of methyl orange adsorption on raw clay from north of Morocco. *J. Environ. Treat. Tech.* **2021**, *9*, 675–685. [CrossRef]
10. Farhat, A.; Zahboune, H.; Lagliti, K.; Fekhaoui, M. The energy potential assessment of controlled landfills in morocco, by dimensioning a dry and discontinuous methanation plant, following the household and similar waste physicochemical characterization results. *J. Environ. Treat. Tech.* **2021**, *9*, 704–713. [CrossRef]
11. Razzaq, A.; Wang, Y.; Chupradit, S.; Suksatan, W.; Shahzad, F. Asymmetric inter-linkages between green technology innovation and consumption-based carbon emissions in BRICS countries using quantile-on-quantile framework. *Technol. Soc.* **2021**, *66*, 101656. [CrossRef]
12. Roshani, M.; Phan, G.T.; Ali, P.J.; Roshani, G.H.; Hanus, R.; Duong, T.; Corniani, E.; Nazemi, E.; Kalmoun, E.M. Evaluation of flow pattern recognition and void fraction measurement in two phase flow independent of oil pipeline's scale layer thickness. *Alex. Eng. J.* **2021**, *60*, 1955–1966. [CrossRef]

13. Yang, W.S.; Park, B.-W.; Jung, E.H.; Jeon, N.J.; Kim, Y.C.; Lee, D.U.; Shin, S.S.; Seo, J.; Kim, E.K.; Noh, J.H. Iodide management in formamidinium-lead-halide–based perovskite layers for efficient solar cells. *Science* **2017**, *356*, 1376–1379. [CrossRef]
14. Manser, J.S.; Christians, J.A.; Kamat, P.V. Intriguing optoelectronic properties of metal halide perovskites. *Chem. Rev.* **2016**, *116*, 12956–13008. [CrossRef]
15. Fu, Y.; Zhu, H.; Schrader, A.W.; Liang, D.; Ding, Q.; Joshi, P.; Hwang, L.; Zhu, X.; Jin, S. Nanowire lasers of formamidinium lead halide perovskites and their stabilized alloys with improved stability. *Nano Lett.* **2016**, *16*, 1000–1008. [CrossRef] [PubMed]
16. Eperon, G.E.; Stranks, S.D.; Menelaou, C.; Johnston, M.B.; Herz, L.M.; Snaith, H.J. Formamidinium lead trihalide: A broadly tunable perovskite for efficient planar heterojunction solar cells. *Energy Environ. Sci.* **2014**, *7*, 982–988. [CrossRef]
17. Roshani, M.; Phan, G.; Roshani, G.H.; Hanus, R.; Nazemi, B.; Corniani, E.; Nazemi, E. Combination of X-ray tube and GMDH neural network as a nondestructive and potential technique for measuring characteristics of gas-oil–water three phase flows. *Measurement* **2021**, *168*, 108427. [CrossRef]
18. Roshani, M.; Phan, G.; Faraj, R.H.; Phan, N.H.; Roshani, G.H.; Nazemi, B.; Corniani, E.; Nazemi, E. Proposing a gamma radiation based intelligent system for simultaneous analyzing and detecting type and amount of petroleum by-products. *Nucl. Eng. Technol.* **2021**, *53*, 1277–1283. [CrossRef]
19. Roshani, M.; Sattari, M.A.; Ali, P.J.; Roshani, G.H.; Nazemi, B.; Corniani, E.; Nazemi, E. Application of GMDH neural network technique to improve measuring precision of a simplified photon attenuation based two-phase flowmeter. *Flow Meas. Instrum.* **2020**, *75*, 101804. [CrossRef]
20. Karami, A.; Roshani, G.H.; Khazaei, A.; Nazemi, E.; Fallahi, M. Investigation of different sources in order to optimize the nuclear metering system of gas–oil–water annular flows. *Neural Comput. Appl.* **2020**, *32*, 3619–3631. [CrossRef]
21. Mahmood, S.S.; Atiya, A.J.; Abdulrazzak, F.H.; Alkaim, A.F.; Hussein, F.H. A Review on applications of carbon nanotubes (cnts) in solar cells. *J. Med. Chem. Sci.* **2021**, *4*, 225–229. [CrossRef]
22. Opeyemi, O.M.; Louis, H.; Oparab, C.I.; Funmilayo, O.O.; Magu, T.O. Porphyrin and phthalocyanines-based solar cells: Fundamental mechanisms and recent advances. *Adv. J. Chem. A* **2019**, *2*, 21–44. [CrossRef]
23. Sun, Q.; Lin, D.; Khayatnezhad, M.; Taghavi, M. Investigation of phosphoric acid fuel cell, linear Fresnel solar reflector and Organic Rankine Cycle polygeneration energy system in different climatic conditions. *Process Saf. Environ. Prot.* **2021**, *147*, 993–1008. [CrossRef]
24. Alghamdi, S.; Asif, M. Pyridazine derivatives act as phosphodiesterase-III, IV, and V Inhibitors. *J. Appl. Organomet. Chem.* **2021**, *1*, 116–124. [CrossRef]
25. Akhir, E.A.P.; Bachok, R.; Arshad, N.I.; Zamri, A.A. Conceptual framework for SIDS alert system. In Proceedings of the 4th International Conference on Computer and Information Sciences (ICCOINS 2018), Kuala Lumpur, Malaysia, 13–14 August 2018; pp. 1–5.
26. Al-Sanjary, O.I.; Ahmed, A.A.; Jaharadak, A.A.B.; Ali, M.A.; Zangana, H.M. Detection clone an object movement using an optical flow approach. In Proceedings of the 2018 Symposium on Computer Applications & Industrial Electronics (ISCAIE 2018), Penang, Malaysia, 28–29 April 2018; IEEE: Manhattan, NY, USA, 2018; pp. 388–394.
27. Ni, J.; Zhuang, X.; Wahab, M.A. Review on the prediction of residual stress in welded steel components. *Comput. Mater. Contin.* **2020**, *62*, 495–523. [CrossRef]
28. Kang, S.; Park, T. Detecting outlier behavior of game player players using multimodal physiology data. *Intell. Autom. Soft Comput.* **2020**, *26*, 205–214. [CrossRef]
29. Kaur, S.; Joshi, V.K. Hybrid soft computing technique based trust evaluation protocol for wireless sensor networks. *Intell. Autom. Soft Comput.* **2020**, *26*, 217–226. [CrossRef]
30. Sharma, M.; Pham, H.; Singh, V. Modeling and analysis of leftover issues and release time planning in multi-release open source software using entropy based measure. *Comput. Syst. Sci. Eng.* **2019**, *34*, 33–46. [CrossRef]
31. Vengadeswaran, S.; Balasundaram, S.R. Core—An optimal data placement strategy in hadoop for data intentitive applications based on cohesion relation. *Comput. Syst. Sci. Eng.* **2019**, *34*, 47–60. [CrossRef]
32. Liao, K.; Yang, Y.-F.; Li, Y.; Sanders, J.N.; Houk, K.; Musaev, D.G.; Davies, H.M. Design of catalysts for site-selective and enantioselective functionalization of non-activated primary C–H bonds. *Nat. Chem.* **2018**, *10*, 1048–1055. [CrossRef]
33. Pang, S.; Hu, H.; Zhang, J.; Lv, S.; Yu, Y.; Wei, F.; Qin, T.; Xu, H.; Liu, Z.; Cui, G. $NH_2CH{=}NH_2PbI_3$: An alternative organolead iodide perovskite sensitizer for mesoscopic solar cells. *Chem. Mater.* **2014**, *26*, 1485–1491. [CrossRef]
34. Ecker, B.; Nolasco, J.C.; Pallarés, J.; Marsal, L.F.; Posdorfer, J.; Parisi, J.; von Hauff, E. Degradation effects related to the hole transport layer in organic solar cells. *Adv. Funct. Mater.* **2011**, *21*, 2705–2711. [CrossRef]
35. Zhang, D.; Chen, X.; Li, F.; Sangaiah, A.K.; Ding, X. Seam-carved image tampering detection based on the cooccurrence of adjacent lbps. *Secur. Commun. Netw.* **2020**, *2020*, 8830310. [CrossRef]
36. Song, Y.; Zhang, D.; Tang, Q.; Tang, S.; Yang, K. Local and nonlocal constraints for compressed sensing video and multi-view image recovery. *Neurocomputing* **2020**, *406*, 34–48. [CrossRef]
37. Zhou, S.; Qiu, J. Enhanced SSD with interactive multi-scale attention features for object detection. *Multimed. Tools Appl.* **2021**, *80*, 11539–11556. [CrossRef]
38. Tang, Q.; Wang, K.; Yang, K.; Luo, Y.S. Congestion-balanced and welfare-maximized charging strategies for electric vehicles. *IEEE Trans. Parallel Distrib. Syst.* **2020**, *31*, 2882–2895. [CrossRef]

39. Wang, J.; Chen, W.; Ren, Y.; Alfarraj, O.; Wang, L. Blockchain based data storage mechanism in cyber physical system. *J. Internet Technol.* **2020**, *21*, 1681–1689.
40. Song, Y.; Li, J.; Chen, X.; Zhang, D.; Tang, Q.; Yang, K. An efficient tensor completion method via truncated nuclear norm. *J. Vis. Commun. Image Represent.* **2020**, *70*, 102791. [CrossRef]
41. Wang, J.; Wu, W.; Liao, Z.; Jung, Y.W.; Kim, J.U. An enhanced PROMOT algorithm with D2D and robust for mobile edge computing. *J. Internet Technol.* **2020**, *21*, 1437–1445.
42. Kenli, L.; Wangdong, Y.; Keqin, L. A hybrid parallel solving algorithm on GPU for quasi-tridiagonal system of linear equations. *IEEE Trans. Parallel Distributed Syst.* **2016**, *27*, 2795–2808.
43. Kenli, L.; Xiaoyong, T.; Bharadwaj, V.; Keqin, L. Scheduling precedence constrained stochastic tasks on heterogeneous cluster systems. *IEEE Trans. Comput.* **2015**, *64*, 191–204.
44. Wangdong, Y.; Kenli, L.; Zeyao, M.; Keqin, L. Performance optimization using partitioned SpMV on GPUs and multicore CPUs. *IEEE Trans. Comput.* **2015**, *64*, 2623–2636.
45. Jing, M.; Kenli, L.; Aijia, O.; Keqin, L. A profit maximization scheme with guaranteed quality of service in cloud computing. *IEEE Trans. Comput.* **2015**, *64*, 3064–3078.
46. Kenli, L.; Wangdong, Y.; Keqin, L. Performance analysis and optimization for SpMV on GPU using probabilistic modeling. *IEEE Trans. Parallel Distrib. Syst.* **2015**, *26*, 196–205.
47. Kenli, L.; Wei, A.; Zhuo, T.; Fan, Z.; Lingang, J.; Keqin, L.; Kai, H. Hadoop recognition of biomedical named entity using conditional random fields. *IEEE Trans. Parallel Distrib. Syst.* **2015**, *26*, 3040–3051.
48. Wang, D.; Chen, X.; Fang, X.; Tang, J.; Lin, F.; Wang, X.; Liu, G.; Liao, L.; Ho, J.C.; Wei, Z. Photoresponse improvement of mixed-dimensional 1D–2D GaAs photodetectors by incorporating constructive interface states. *Nanoscale* **2021**, *13*, 1086–1092. [CrossRef]
49. Ji, B.; Zhang, F.; Song, X.; Tang, Y. A novel potassium-ion-based dual-ion battery. *Adv. Mater.* **2017**, *29*, 1700519. [CrossRef]
50. Kim, H.-S.; Lee, C.-R.; Im, J.-H.; Lee, K.-B.; Moehl, T.; Marchioro, A.; Moon, S.-J.; Humphry-Baker, R.; Yum, J.-H.; Moser, J.E. Lead iodide perovskite sensitized all-solid-state submicron thin film mesoscopic solar cell with efficiency exceeding 9%. *Sci. Rep.* **2012**, *2*, 591. [CrossRef]
51. Wang, M. Exploring stability of formamidinium lead trihalide for solar cell application. *Sci. Bull.* **2017**, *62*, 249–255. [CrossRef]
52. Yuming, X.; Kenli, L.; Ligang, H.; Longxin, Z.; Keqin, L. A hybrid chemical reaction optimization scheme for task scheduling on heterogeneous computing systems. *IEEE Trans. Parallel Distrib. Syst.* **2015**, *26*, 3208–3222.
53. Kenli, L.; Weihua, Z.; Keqin, L. A fast algorithm with less operations for length-N = q × 2m DFTs. *IEEE Trans. Signal Process.* **2015**, *63*, 673–683.
54. Kenli, L.; Xiaoyong, T.; Keqin, L. Energy-efficient stochastic task scheduling on heterogeneous computing systems. *IEEE Trans. Parallel Distributed Syst.* **2014**, *25*, 2867–2876.
55. Xiaoyong, T.; Kenli, L.; Zeng, Z.; Bharadwaj, V. A novel security-driven scheduling algorithm for precedence-constrained tasks in heterogeneous distributed systems. *IEEE Trans. Comput.* **2011**, *60*, 1017–1029. [CrossRef]
56. Davarpanah, A. Parametric study of polymer-nanoparticles-assisted injectivity performance for axisymmetric two-phase flow in EOR processes. *Nanomaterials* **2020**, *10*, 1818. [CrossRef]
57. Zhang, D.; Wang, S.; Li, F.; Tian, S.; Wang, J.; Ding, X.; Gong, R. An efficient ECG denoising method based on empirical mode decomposition, sample entropy, and improved threshold function. *Wirel. Commun. Mob. Comput.* **2020**, *2020*, 8811962. [CrossRef]
58. Tang, Q.; Wang, K.; Song, Y.; Li, F.; Park, J.H. Waiting time minimized charging and discharging strategy based on mobile edge computing supported by software-defined network. *IEEE Internet Things J.* **2019**, *7*, 6088–6101. [CrossRef]
59. Zhang, J.; Yang, K.; Xiang, L.; Luo, Y.; Xiong, B.; Tang, Q. A self-adaptive regression-based multivariate data compression scheme with error bound in wireless sensor networks. *Int. J. Distrib. Sens. Netw.* **2013**, *9*, 913497. [CrossRef]
60. Zhang, J.; Sun, J.; Wang, J.; Yue, X.G. Visual object tracking based on residual network and cascaded correlation filters. *J. Ambient Intell. Humaniz. Comput.* **2021**, *12*, 8427—8440. [CrossRef]
61. Gu, K.; Wang, Y.; Wen, S. Traceable threshold proxy signature. *J. Inf. Sci. Eng.* **2017**, *33*, 63–79.
62. Li, W.; Ding, Y.; Yang, Y.; Sherratt, R.S.; Park, J.H.; Wang, J. Parameterized algorithms of fundamental NP-hard problems: A survey. *Hum. Cent. Comput. Inf. Sci.* **2017**, *10*, 29. [CrossRef]
63. Gu, K.; Yang, L.; Wang, Y.; Wen, S. Traceable identity-based group signature. *RAIRO Theor. Inform. Appl.* **2016**, *50*, 193–226. [CrossRef]
64. Even, J.; Pedesseau, L.; Katan, C.; Kepenekian, M.; Lauret, J.-S.; Sapori, D.; Deleporte, E. Solid-state physics perspective on hybrid perovskite semiconductors. *J. Phys. Chem. C* **2015**, *119*, 10161–10177. [CrossRef]
65. Egger, D.A.; Rappe, A.M.; Kronik, L. Hybrid organic–inorganic perovskites on the move. *Acc. Chem. Res.* **2016**, *49*, 573–581. [CrossRef]
66. Zhou, B.; Liu, Z.; Li, C.; Liu, M.; Jiang, L.; Zhou, Y.; Zhou, F.L.; Chen, S.; Jerrams, S.; Yu, J. A highly stretchable and sensitive strain sensor based on dopamine modified electrospun SEBS fibers and MWCNTs with carboxylation. *Adv. Electron. Mater.* **2021**, *7*, 2100233. [CrossRef]
67. Yin, B.; Zhou, S.; Lin, Y.; Liu, Y.; Hu, Y. Efficient distributed skyline computation using dependency-based data partitioning. *J. Syst. Softw.* **2014**, *93*, 69–83. [CrossRef]

68. Long, M.; Xiao, X. Outage performance of double-relay cooperative transmission network with energy harvesting. *Phys. Commun.* **2018**, *29*, 261–267. [CrossRef]
69. Xu, Z.; Liang, W.; Li, K.C.; Xu, J.; Jin, H. A blockchain-based roadside unit-assisted authentication and key agreement protocol for internet of vehicles. *J. Parallel Distrib. Comput.* **2021**, *149*, 29–39. [CrossRef]
70. Wang, W.; Yang, Y.; Li, J.; Hu, Y.; Luo, Y.; Wang, X. Woodland labeling in chenzhou, China, via deep learning approach. *Int. J. Comput. Intell. Syst.* **2020**, *13*, 1393–1403. [CrossRef]
71. Qu, Y.; Xiong, N. RFH: A resilient, fault-tolerant and high-efficient replication algorithm for distributed cloud storage. In Proceedings of the 41st International Conference on Parallel Processing, Pittsburgh, PA, USA, 10–13 September 2012; pp. 520–529.
72. Fang, W.; Yao, X.; Zhao, X.; Yin, J.; Xiong, N. A stochastic control approach to maximize profit on service provisioning for mobile cloudlet platforms. *IEEE Trans. Syst. Man Cybern.* **2016**, *48*, 522–534. [CrossRef]
73. Zhang, X.; Tang, Y.; Zhang, F.; Lee, C.S. A novel aluminum–graphite dualion battery. *Adv. Energy Mater.* **2016**, *6*, 1502588. [CrossRef]
74. Gong, J.; Darling, S.B.; You, F. Perovskite photovoltaics: Life-cycle assessment of energy and environmental impacts. *Energy Environ. Sci.* **2015**, *8*, 1953–1968. [CrossRef]
75. Mattoni, A.; Filippetti, A.; Saba, M.; Delugas, P. Methylammonium rotational dynamics in lead halide perovskite by classical molecular dynamics: The role of temperature. *J. Phys. Chem. C* **2015**, *119*, 17421–17428. [CrossRef]
76. Noh, J.H.; Im, S.H.; Heo, J.H.; Mandal, T.N.; Seok, S.I. Chemical management for colorful, efficient, and stable inorganic–organic hybrid nanostructured solar cells. *Nano Lett.* **2013**, *13*, 1764–1769. [CrossRef]
77. Schmidt, L.C.; Pertegás, A.; González-Carrero, S.; Malinkiewicz, O.; Agouram, S.; Minguez Espallargas, G.; Bolink, H.J.; Galian, R.E.; Pérez-Prieto, J. Nontemplate synthesis of $CH_3NH_3PbBr_3$ perovskite nanoparticles. *J. Am. Chem. Soc.* **2014**, *136*, 850–853. [CrossRef]
78. Zhang, F.; Yang, B.; Zheng, K.; Yang, S.; Li, Y.; Deng, W.; He, R. Formamidinium lead bromide ($FAPbBr_3$) perovskite microcrystals for sensitive and fast photodetectors. *Nano Micro Lett.* **2018**, *10*, 43. [CrossRef] [PubMed]
79. Yousefpour, P.; McDaniel, J.R.; Prasad, V.; Ahn, L.; Li, X.; Subrahmanyan, R.; Weitzhandler, I.; Suter, S.; Chilkoti, A. Genetically encoding albumin binding into chemotherapeutic-loaded polypeptide nanoparticles enhances their antitumor efficacy. *Nano Lett.* **2018**, *18*, 7784–7793. [CrossRef] [PubMed]
80. Zhumekenov, A.A.; Saidaminov, M.I.; Haque, M.A.; Alarousu, E.; Sarmah, S.P.; Murali, B.; Dursun, I.; Miao, X.-H.; Abdelhady, A.L.; Wu, T. Formamidinium lead halide perovskite crystals with unprecedented long carrier dynamics and diffusion length. *ACS Energy Lett.* **2016**, *1*, 32–37. [CrossRef]
81. Giorgi, G.; Fujisawa, J.-I.; Segawa, H.; Yamashita, K. Cation role in structural and electronic properties of 3D organic–inorganic halide perovskites: A DFT analysis. *J. Phys. Chem. C* **2014**, *118*, 12176–12183. [CrossRef]
82. Levchuk, I.; Osvet, A.; Tang, X.; Brandl, M.; Perea, J.D.; Hoegl, F.; Matt, G.J.; Hock, R.; Batentschuk, M.; Brabec, C.J. Brightly luminescent and color-tunable formamidinium lead halide perovskite FAPbX3 (X = Cl, Br, I) colloidal nanocrystals. *Nano Lett.* **2017**, *17*, 2765–2770. [CrossRef]
83. Chen, Q.; De Marco, N.; Yang, Y.M.; Song, T.-B.; Chen, C.-C.; Zhao, H.; Hong, Z.; Zhou, H.; Yang, Y. Under the spotlight: The organic–inorganic hybrid halide perovskite for optoelectronic applications. *Nano Today* **2015**, *10*, 355–396. [CrossRef]
84. Mannino, G.; Deretzis, I.; Smecca, E.; La Magna, A.; Alberti, A.; Ceratti, D.; Cahen, D. Temperature-dependent optical band gap in $CsPbBr_3$, $MAPbBr_3$, and $FAPbBr_3$ single crystals. *J. Phys. Chem. Lett.* **2020**, *11*, 2490–2496. [CrossRef] [PubMed]
85. Zhao, M.; Shi, Y.; Dai, J.; Lian, J. Ellipsometric study of the complex optical constants of a $CsPbBr_3$ perovskite thin film. *J. Mater. Chem. C* **2018**, *6*, 10450–10455. [CrossRef]
86. Walters, G.; Sutherland, B.R.; Hoogland, S.; Shi, D.; Comin, R.; Sellan, D.P.; Bakr, O.M.; Sargent, E.H. Two-photon absorption in organometallic bromide perovskites. *ACS Nano* **2015**, *9*, 9340–9346. [CrossRef]
87. Zhang, W.; Saliba, M.; Moore, D.T.; Pathak, S.K.; Hörantner, M.T.; Stergiopoulos, T.; Stranks, S.D.; Eperon, G.E.; Alexander-Webber, J.A.; Abate, A. Ultrasmooth organic–inorganic perovskite thin-film formation and crystallization for efficient planar heterojunction solar cells. *Nat. Commun.* **2015**, *6*, 6142. [CrossRef]
88. Ceratti, D.R.; Rakita, Y.; Cremonesi, L.; Tenne, R.; Kalchenko, V.; Elbaum, M.; Oron, D.; Potenza, M.A.C.; Hodes, G.; Cahen, D. Self-healing inside $APbBr_3$ halide perovskite crystals. *Adv. Mater.* **2018**, *30*, 1706273. [CrossRef]
89. Zheng, X.; Wu, C.; Jha, S.K.; Li, Z.; Zhu, K.; Priya, S. Improved phase stability of formamidinium lead triiodide perovskite by strain relaxation. *ACS Energy Lett.* **2016**, *1*, 1014–1020. [CrossRef]
90. Thote, A.; Jeon, I.; Lee, J.-W.; Seo, S.; Lin, H.-S.; Yang, Y.; Daiguji, H.; Maruyama, S.; Matsuo, Y. Stable and reproducible 2D/3D formamidinium–lead–iodide perovskite solar cells. *ACS Appl. Energy Mater.* **2019**, *2*, 2486–2493. [CrossRef]
91. Mannino, G.; Deretzis, I.; Smecca, E.; Giannazzo, F.; Valastro, S.; Fisicaro, G.; La Magna, A.; Ceratti, D.; Alberti, A. $CsPbBr_3$, $MAPbBr_3$, and $FAPbBr_3$ Bromide perovskite single crystals: Interband critical points under dry N_2 and optical degradation under humid air. *J. Phys. Chem. C* **2021**, *125*, 4938–4945. [CrossRef]
92. Shcherbakov-Wu, W.; Sercel, P.C.; Krieg, F.; Kovalenko, M.V.; Tisdale, W.A. Temperature-independent dielectric constant in $CsPbBr_3$ nanocrystals revealed by linear absorption spectroscopy. *J. Phys. Chem. Lett.* **2021**, *12*, 8088–8095. [CrossRef]
93. Jiang, Q.; Zhao, Y.; Zhang, X.; Yang, X.; Chen, Y.; Chu, Z.; Ye, Q.; Li, X.; Yin, Z.; You, J. Surface passivation of perovskite film for efficient solar cells. *Nat. Photonics* **2019**, *13*, 460–466. [CrossRef]

94. Tong, Y.-L.; Zhang, Y.-W.; Ma, K.; Cheng, R.; Wang, F.; Chen, S. One-step synthesis of FA-directing $FAPbBr_3$ perovskite nanocrystals toward high-performance display. *ACS Appl. Mater. Interfaces* **2018**, *10*, 31603–31609. [CrossRef]
95. Govinda, S.; Kore, B.P.; Swain, D.; Hossain, A.; De, C.; Guru Row, T.N.; Sarma, D. Critical comparison of $FAPbX_3$ and $MAPbX_3$ (X = Br and Cl): How do they differ? *J. Phys. Chem. C* **2018**, *122*, 13758–13766. [CrossRef]
96. Seo, J.; Noh, J.H.; Seok, S.I. Rational strategies for efficient perovskite solar cells. *Acc. Chem. Res.* **2016**, *49*, 562–572. [CrossRef] [PubMed]
97. Kanno, S.; Imamura, Y.; Hada, M. Theoretical study on rotational controllability of organic cations in organic–inorganic hybrid perovskites: Hydrogen bonds and halogen substitution. *J. Phys. Chem. C* **2017**, *121*, 26188–26195. [CrossRef]
98. Fang, H.; Jena, P. Molecular origin of properties of organic–inorganic hybrid perovskites: The big picture from small clusters. *J. Phys. Chem. Lett.* **2016**, *7*, 1596–1603. [CrossRef]
99. Weller, M.T.; Weber, O.J.; Frost, J.M.; Walsh, A. Cubic perovskite structure of black formamidinium lead iodide, α-$[HC(NH_2)_2]PbI_3$, at 298 K. *J. Phys. Chem. Lett.* **2015**, *6*, 3209–3212. [CrossRef]
100. Maheshwari, S.; Fridriksson, M.B.; Seal, S.; Meyer, J.R.; Grozema, F.C. The relation between rotational dynamics of the organic cation and phase transitions in hybrid halide perovskites. *J. Phys. Chem. C* **2019**, *123*, 14652–14661. [CrossRef]
101. Johnston, A.; Walters, G.; Saidaminov, M.I.; Huang, Z.; Bertens, K.; Jalarvo, N.; Sargent, E.H. Bromine incorporation and suppressed cation rotation in mixed-halide perovskites. *ACS Nano* **2020**, *14*, 15107–15118. [CrossRef] [PubMed]
102. Sharma, V.; Mukhopadhyay, R.; Mohanty, A.; Tyagi, M.; Embs, J.; Sarma, D. Contrasting behaviors of FA and MA cations in a $PbBr_3$. *J. Phys. Chem. Lett.* **2020**, *11*, 9669–9679. [CrossRef]
103. Mosconi, E.; Quarti, C.; Ivanovska, T.; Ruani, G.; De Angelis, F. Structural and electronic properties of organo-halide lead perovskites: A combined IR-spectroscopy and ab initio molecular dynamics investigation. *Phys. Chem. Chem. Phys.* **2014**, *16*, 16137–16144. [CrossRef]
104. Giannozzi, P.; Baroni, S.; Bonini, N.; Calandra, M.; Car, R.; Cavazzoni, C.; Ceresoli, D.; Chiarotti, G.L.; Cococcioni, M.; Dabo, I. QUANTUM ESPRESSO: A modular and open-source software project for quantum simulations of materials. *J. Phys. Condens. Matter* **2009**, *21*, 395502. [CrossRef] [PubMed]
105. Batsanov, S.S. Van der Waals radii of elements. *Inorg. Mater.* **2001**, *37*, 871–885. [CrossRef]
106. Davarpanah, A. The feasible visual laboratory investigation of formate fluids on the rheological properties of a shale formation. *Int. J. Environ. Sci. Technol.* **2019**, *16*, 4783–4792. [CrossRef]